ELSEVIER

Contents lists available at ScienceDirect

Applied Materials Today

journal homepage: www.elsevier.com/locate/apmt



Casting of high surface area electrodes enabled by low-temperature welding of copper nanoporous powders and nanoparticles hybrid feedstocks

Stanislau Niauzorau , Natalya Kublik , Emmanuel Dasinor , Amm Hasib , Aliaksandr Sharstniou , Bruno Azeredo *

Arizona State University, Ira A. Fulton Schools of Engineering - The School of Manufacturing Systems and Networks, 6075 S. Innovation Way West, Mesa, AZ 85212

ARTICLE INFO

Keywords: Dealloying Powder metallurgy Additive manufacturing Nanoporous metals Nanoscale welding

ABSTRACT

Nanoporous metallic powders are proposed as electrodes for hydrogen production, current collectors in batteries, or active material in propellants to overcome limitations in reaction kinetics of their bulk solid counterpart. However, their consolidation into 3D parts via powder metallurgy while maintaining high mechanical performance is limited by their thermodynamic instability during sintering and poor flowability. This paper demonstrates the synthesis of spherical nanoporous copper powders (PCu) via dealloying of Cu-Al gas-atomized precursors with high-throughput (i.e., 0.1 kg/hr), moderate flowability (i.e., Carney flowrate of 32.9 s/50 g), moderate-oxygen content (i.e., < 12 at.%), high-surface area (\sim 12 m²/g) and free of precipitates. The nanoscale weldability of hybrid feedstocks composed of PCu (65.5 – 91.2 vol.%) and copper nanoparticles (8.8 – 34.5 vol.%) were harvested to sinter them at temperatures as low as a third of its melting point and overcome the metastability of PCu to preserve its high-surface area. Open-die casting in reducing atmospheres was employed at temperatures between 300 – 700 °C resulting in parts with ultimate compression strength of 3.6 – 17.8 MPa while forming electrically conductive solids with preserved nanoporosity (i.e., pore size 24 – 36 nm). Such feedstocks may be integrated with powder-based manufacturing processes such as powder injection molding and additive manufacturing to produce complex architectures.

1. Introduction

In recent years, nanoporous metal powder (NPMP) is a particularly attractive feedstock for its integrability with powder metallurgy processes [1,2] such as powder casting or additive manufacturing (AM) as it holds the potential to fabricate electrically conductive high-surface area electrodes [3,4] with complex multifunctional architectures [5] such as 3D lattices and interdigitated structures for high powder density batteries. [6] However, this integration remains underexplored since methods for kilogram-scale production of NPMP are limited in material selection or throughput, and fundamental studies on nanoscale metal welding [7] have not been translated into powder metallurgy applications to sinter NPMP while preserving its porosity since the latter is metastable at temperatures as low as 10-30% of its melting temperature. [8]

State-of-the-art NPMP production methods include (i) combustion synthesis of metallic alloys, [9–11] (ii) directed- (e.g., two photon lithography) [12] or self-assembly (e.g., block-copolymers [13] and

capillary assembly of nanospheres) [14,15] of sacrificial templates combined with metal deposition methods, [16] (iii) dealloying of powder precursor alloys made by ball-milling, gas- or plasma-atomization [1,17], and (iv) ball milling of dealloyed thin-films, foils or other bulk formats. However, to be integrated with powder metallurgy, NPMP require high-volume production (i.e., kg/hr), morphology control such as powder size distribution, superior spheroidicity and dispersion to prevent interlocking and agglomerates, and yield a flowable feedstock at scale. Combustion synthesis offers high throughput, but low surface area (i.e., $0.8 - 3.5 \text{ m}^2/\text{g}$) [11] due to high processing pressures and temperatures. Dealloying of plated hollow, [18] ball milled [19-21] and gas atomized [1,22,23] powder alloys can yield small pore sizes which is only dependent on its thermodynamic limitations (e.g., adatom diffusion rate and coarsening). [24,25] Due to irregular particle shapes and wide size distribution, ball milling can lead to poor flowability and particle interlocking resulting in low powder packing factor and porosity in the final part. Also, the use of dealloyed hollow metal particles would result in low density of the part. Therefore,

E-mail address: bruno.azeredo@asu.edu (B. Azeredo).

^{*} Corresponding author.

the use of NPMP derived from gas-atomized powders is a preferred choice for integrating with either powder casting methods (e.g., open-die casting and powder injection molding) or powder-based metal additive technologies (e.g., selective laser melting, metal fused filament fabrication, binder jetting, and directed energy deposition) making it necessary to study process-structure relationships for its synthesis and its weldability.

In thin-film formats, process-structure relationships for dealloyed nanoporous metals have been extensively studied [26] owing to easy access to a wide selection of alloy compositions via physical vapor deposition [27] and cold rolling [28] methods. However, in powder formats, synthesis of NPMP faces the following roadblocks: (i) limited selection of suitable precursor alloy compositions and phases due to rapid solidification during its production (e.g., gas-atomization) and costs associated with small batch production for R&D, (ii) incompatibility of powders with electrolytic forms of dealloying which limits control of reaction kinetics and pore sizes, [29,30] (iii) exothermic reactions leading to an uncontrollable and hazardous thermal runaway [31] due to its large surface-to-volume ratio, (iv) undesirable precipitate formation (e.g., metal hydroxides), [32] and (v) high reactivity with atmospheric oxygen and nitrogen leading to limited air-handling capability which requires passivation strategies for non-noble NPMP (i.e., Cu, Ni, Al, etc.) or handling in costly inert environments. Despite these limitations, NPMP has a growing interest in the community [1,33,34] since, during dealloying, its spheroidicity is preserved [35] (i.e., when gas-atomized feedstock is used) and powders shrink freely without forming cracks compared to precursors that are constrained by a substrate. [36]

To integrate NPMP into powder metallurgy and fabricate nanoporous conductive metal parts, a key fundamental requirement is to weld them while preserving its porosity. Nanoporous metals are metastable at onset temperatures as low as one-tenth of its melting point and undergo a thermal coarsening process that is both time- and temperature-dependent. [37] For example, recent work exploited the high-pressures (e.g., \sim 20 MPa), rapid heating (e.g., 100 °C/min) and cooling cycle of spark plasma sintering to promote necking and weld spherical nanoporous copper powders (PCu) [38] while heating it up to maximum temperatures lower than 550 °C, producing low-surface area solids with ligament sizes of \sim 480 nm and high strength parts (i.e., ultimate compression strength of $\sim 50 - 150$ MPa). Another important element of successful metal-to-metal welding is the management and removal of the oxides for non-noble metals both before sintering when the powders are removed from dealloving solution and during its sintering cycle. For example, reducing atmospheres have been used to remove common copper oxides (e.g., Cu₂O and CuO) from Cu nanoparticles at temperatures as low as 300 and 280 °C respectively; [39] functional passivation strategies were used for Cu such as polymer nanocoatings whose decomposition products serve to reduce these oxides during photonic sintering in atmospheric conditions; [40] or handling the entire process flow under inert atmosphere is an option. To date, most of the recent efforts in literature were focused on either dealloying of 3D printed alloy precursors [2,41-43] or electroplating 3D nanoscale templates [43,44] with limited efforts in integrating NPMP into powder metallurgy. The former approach has failed to yield any mechanical data of its specimens and is plagued by residual stresses caused by the dealloying process itself.

In this study, solid and electrically conductive copper parts are produced by exploiting Ostwald ripening and nanoscale welding between NPMP and their mixtures containing Cu nanoparticles at sintering temperatures as low as 28% of melting temperature of bulk copper. First, the large-scale bulk synthesis (i.e., 0.1~kg/h with a single tabletop 5~L beaker) of PCu powder is investigated by (i) titrating NaOH into a suspension of CuAl powders and water and (ii) by titrating CuAl powders into a NaOH solution. The latter approach is found to avoid the formation of bayerite precipitates and copper oxides (i.e., Cu_2O and CuO) by maintaining high concentrations of NaOH (i.e., 3~M) during dealloying.

Second, its surface passivation with a copper oxide layer by exposing it to ambient conditions and its effect on thermal coarsening of PCu are studied as a function of powder quantity in the beaker with a constant aspect ratio. Third, the hybrid feedstock containing 8.8 to 34.5 vol.% of 300 nm Cu nanoparticles (CuNPs) and PCu powder was fabricated in order to increase the packing density and facilitate nanoscale welding via Ostwald ripening of nanoparticles [45] which promotes necking of the micron-sized PCu powders. Fourth, the hybrid feedstock is subjected to sintering in an open-die graphite mold in reducing atmosphere at a temperature range of 300-700 °C to fabricate electrically conductive parts. Finally, parts were submitted to compression testing achieving a low mechanical strength (i.e., maximum ultimate compression strength of 17.8 MPa) with preserved porosity and ligament sizes ranging between 24 – 36 nm which is attributed to the high thermal stability of PCu ligaments between 300 – 600 °C. NPMP and their mixtures containing Cu nanoparticles have the potential to be broadly extended to powder injection molding and additive manufacturing.

2. Results and discussion

Production scaling of PCu by dealloying of CuAl powder with a large particle size (i.e., $100~nm-30~\mu m$) is hazardous due to its high surface area compared to that of thin films and other bulk formats, and the exothermic nature of the aluminum etching process that can result in an uncontrollable thermal runaway reaction. [31] Steps that are introduced in this study in order to suppress thermal runaway are (i) titration of either etchant or powder precursor and (ii) preheating the solution at the beginning of the experiment.

2.1. Porous copper synthesis

In this section, two approaches for producing oxide-containing PCu powders - with oxygen content greater than 10 at.% - are presented without regards as to whether the oxide formation took place in the etching solution or during exposure of the powder to atmosphere. Also, their role in regulating the formation of precipitates is discussed. The two approaches for dealloying include immersing copper-aluminum (CuAl) powders (i.e., precursor) into an aluminum etching NaOH(aq) solution by: (i) titrating the latter into CuAl powders suspended in DI water until a 3 M solution concentration is reached ('1st approach'), and (ii) titrating CuAl powders in timed intervals into 3 M NaOH $_{\mbox{\scriptsize (aq)}}$ solution ('2nd approach'). Subsequently, the origin of oxide formation is identified to be the exposure to atmospheric conditions and a method for its regulation is presented yielding oxide content as low as 11 ± 1 at.%. Albeit the authors did not find any evidence of Cu dissolution in 3 M NaOH in this study, it is known that Cu can dissolve via an oxygen reduction reaction in activated carbon. [46]

2.1.1. 1st approach: synthesis of nanoporous copper oxide powders decorated with bayerite

Powders obtained using the 1st approach exhibit a nanoporous core (Fig. 1g) whose morphology is characteristic of dealloying and, after vacuum drying and exposure to atmosphere, the XRD data revealed that the core is composed of cuprite (Cu₂O) (Fig. 1i). Cuprite can form (i) during dealloying due to partial oxidation in solution of generated copper adatoms [47] and (ii) after exposure to atmosphere by oxidation of copper. EDS data shows the powder after exposure to air becomes heavily oxidized with 60.2 at.% of oxygen, 29.1 at.% of aluminum and 10.1 at.% of copper. During dealloying of CuAl alloy in both approaches, aluminum is selectively etched with formation of dissolvable sodium aluminate (NaAlO₂) and the reaction is described as follows in Eq. (1):

$$2 Al + 2 NaOH + 2 H2O = 2 NaAlO2 + 3 H2$$
 (1)

However, in the 1st approach, at low concentrations of sodium hydroxide during the onset of titration, aluminum preferably reacts to form

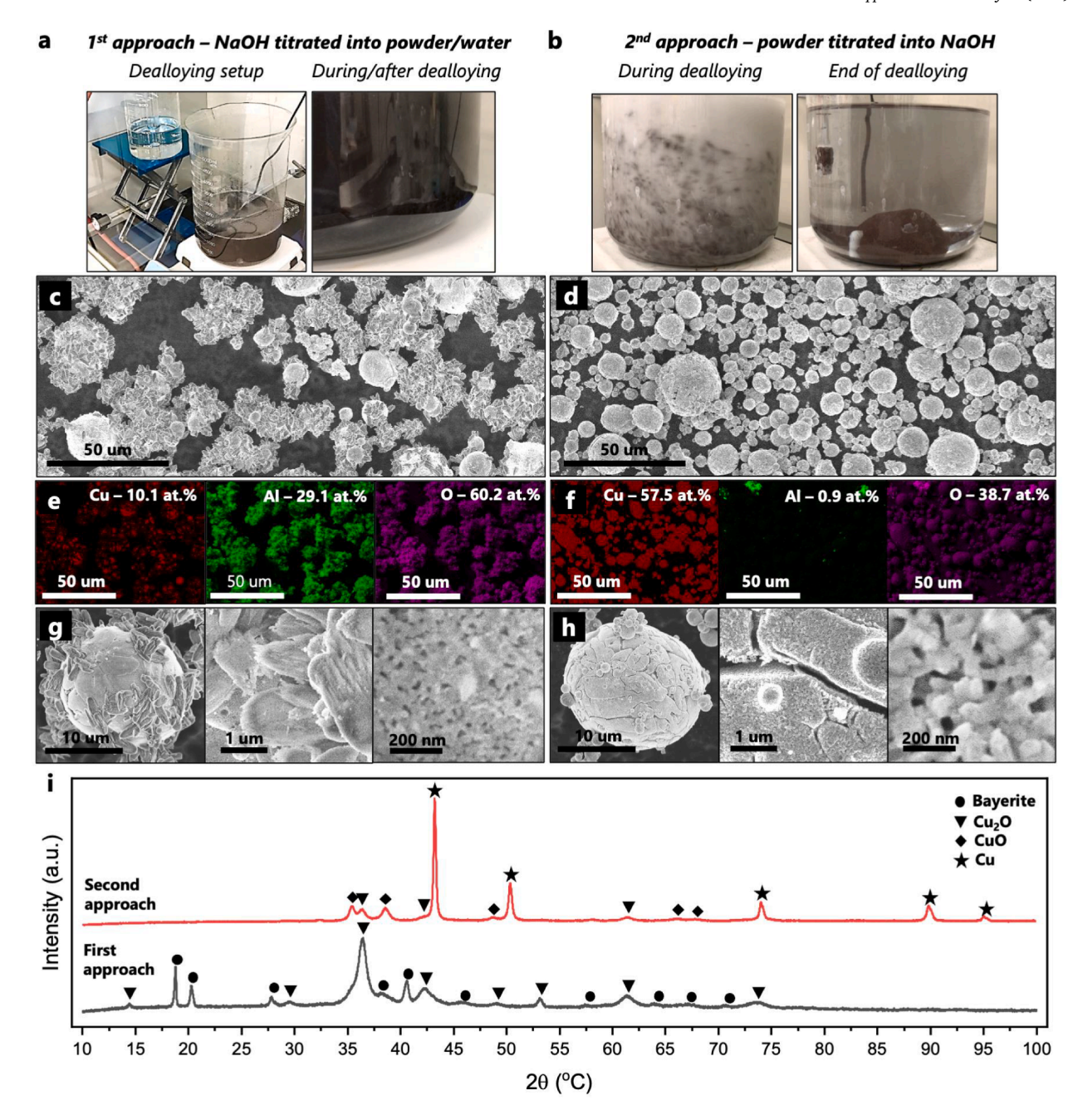


Fig. 1. PCu powders fabricated following 1st and 2nd approaches: photographs of (a, b) dealloying setup and powder suspension in electrolyte, (c, d) Low-magnification SEM images, (e, f) EDS elemental mapping, (g, h) high-magnification SEM images of PCu oxides fabricated by 1st and 2nd approaches respectively. (i) Corresponding XRD analysis of fabricated PCu oxide powders.

aluminum hydroxide (Al(OH) $_3$) via its hydrolysis as shown in Eq. (2):

$$2 Al + 6 H2O = 2Al(OH)3 + 3H2$$
 (2)

Precipitates are evidenced by EDS (Fig. 1e) and XRD (Fig. 1i) analyses which revealed their oxygen and aluminum rich compositions (i.e., 29.1 at.%), and identified their crystal structure of Al(OH) $_3$ to be a single-phase bayerite with the first diffraction peak at 18.739° . [48] Note that no crystalline pure aluminum or its oxides are found in the XRD data suggesting most of it is converted to Al(OH) $_3$ in solution. To contextualize this result with literature, Zhang et al. [32] concluded that tuning the concentration of both aluminum ions and NaOH(aq) can regulate the formation of different Al(OH) $_3$ phases (e.g., boehmite, bayerite or gibbsite). It was found that bayerite is preferably formed when the molarity of Al $_3$ + is 0.1-1 mol/L and NaOH concentration is

0-0.7~M at a solution temperature between 60 and 80 °C. Similarly, in this study the concentrations of NaOH solution and $Al^{3+} \rm increase$ from 0 to 3 M and from 0 to 0.35 mol/L respectively while the solution temperature increases from 50 to 72 °C. During the etching in the 1st approach, the color of the solution becomes dark and opaque which is characteristic of a solution saturated with aluminum hydroxide (Fig. 1a).

2.1.2. 2nd approach: Synthesis of bayerite-free porous copper powders

On one hand, the 1st approach ensures that all powders experience similar etching rate and temperature oscillations while yielding bayerite precipitates. On the other hand, the 2nd approach titrates powder into a highly concentrated NaOH solution which means that, at each iteration of titration, the concentrations of NaOH, pH, Al³⁺ fluctuate which could

lead to non-uniformities in a given batch. At the same time, the chance of forming aluminum hydroxide (see Eq. (2)) in the 2nd approach is minimized due to the high NaOH concentration. Instead, aluminum (i.e., 0.7 mmol/L total at each titration step) reacts with sodium hydroxide (see Eq. (1)) which is consistent with literature [32] resulting into rapid formation of large amounts of sodium aluminate products which is evidenced by its white appearance during dealloying and is followed by its subsequent dissolution into the electrolyte leading to a clear and translucent solution upon the completion of dealloying (Fig. 1b). Note that the white appearance of the etching solution was not observed during synthesis of powders using the 1st approach. According to stoichiometric calculations based on Eq. (1), the amount of NaOH used was 8.5 times greater than what was stoichiometrically required to etch all of the aluminum in the precursor powders in both dealloying approaches (see Supplementary Table S1). Thus, powders obtained using the 2nd approach exhibit nanoporous structure free of precipitates (Fig. 1h) and, after vacuum drying and exposure to atmosphere, XRD data revealed that powders show prominent crystalline Cu peaks at 43.4°, 50.5°, 74.2°, which were absent for powders fabricated following the 1st approach. Moreover, according to EDS data the amount of copper in PCu oxide powders is 57.5 at.% which is 47.4 at.% higher than in bayerite-covered PCu oxide powders from the 1st approach (Fig. 1f).

2.1.3. 2nd approach: Regulation of oxygen incorporation

Although SEM and XRD analysis of oxide-containing PCu powders fabricated following the 2nd approach have not revealed any presence of bayerite (Fig. 1h and i), the powder contains a substantial amount of oxygen (i.e., 38.7 at.%) in the form of Cu₂O and CuO after its exposure to atmosphere (Fig. 2h). In prior literature, oxides have been shown to form both in solution during dealloying [49] and by post-oxidation in atmospheric conditions. [49,50] Therefore, to make a distinction of whether oxides are formed either during dealloying process or after exposure to air, a detailed analysis of the kinetics of PCu oxidation is presented in this section by examining the contributions of the drying process and exposure of powder to atmosphere to its oxygen content.

The oxidation of PCu powder after drying and venting into atmospheric conditions at room temperature (i.e., 20 - 24 °C) is accompanied by rapid heating of the sample whose temperature profile and maximum

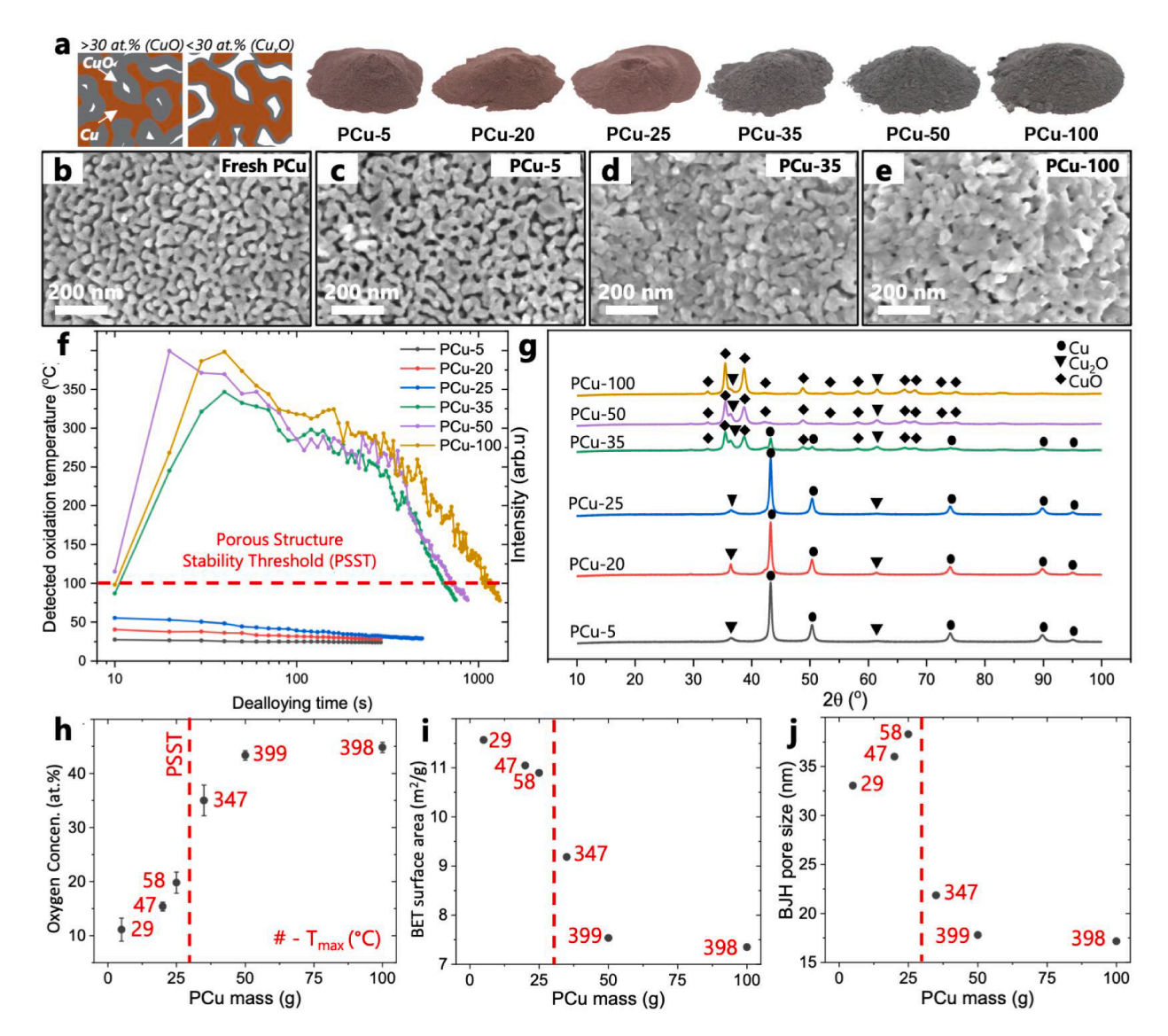


Fig. 2. (a) Photographs showing the color change of PCu powder after drying. The number in the label "PCu-#" corresponds to the mass of PCu powder in grams. Note that the color of PCu powder varies with layer thickness which is indicative of Cu₂O and CuO which are naturally red and black, respectively. SEM micrographs of PCu powders that were (b) wet transferred in alcohol into the SEM chamber for minimal oxygen exposure, (c) PCu-5, (d) PCu-35 and (e) PCu-100. Graphs showing (f) temperature history of PCu powders during first exposure to atmosphere, and its corresponding (g) oxide structure from XRD, (h) oxygen concentration from EDS, (i) surface area from BET and (j) pore size from BJH.

temperature (T_{max}) were recorded with an infrared thermometer gun (Fig. 2f). This increase in temperature can be either moderate (i.e., T_{max} < 55 °C) when heat can dissipate at a high rate, or extreme (i.e., T_{max} > 325 °C) when an uncontrollable high-temperature exothermic runaway (HT-ER) takes place. In the latter scenario, temperatures are higher than the porous structure stability threshold (PSST) (Fig. 2f) and PCu powder begins to thermally coarsen which is confirmed with DSC analysis (i.e., the onset of thermal coarsening is 95 - 100 °C for PCu). [51,52] In theory, this temperature rise regulates the rate and total amount of oxygen incorporation since the oxygen diffusion constant follows an Arrhenius dependence with temperature. [53] To test this hypothesis, the rate of heat dissipation was varied by increasing the surface area to volume ratio of the powder in the beaker either (i) by increasing its aspect ratio at a constant quantity of the powder or (ii) by decreasing the thickness of the powder layer in a beaker by reducing its quantity per beaker. In the first approach, its aspect ratio was varied from 1.5 to 0.12 for a fixed amount of 25 g of PC (i.e., PCu-25), and it was possible to reduce the final oxygen content from 38.7 (Fig. 1h) to 19.8 at.% (Fig. 2h) and T_{max} from 350 to 55 °C. Second, by decreasing the powder quantity in a given beaker and, consequently, its layer thickness from 6 mm (i.e., PCu-100) to 0.3 mm (i.e., PCu-5), it was possible to reduce the oxygen level from 44.8 ± 1.0 to 11.1 ± 2.1 at.% (Fig. 2h) and T_{max} from 399 to 27 °C respectively. Note that the core-shell structure is only preserved for PCu powder with oxygen content below 40 at.% (i.e., for PCu-5, PCu-20, PCu-25 and PCu-35), and that PCu-50 and PCu-100 are fully oxidized to CuO without the presence of crystalline Cu according to XRD analysis (Fig. 2g), [54]

The presence of the HT-ER not only regulates oxygen incorporation, but also the type of oxide (Cu₂O or CuO) that is formed as evidenced (i) by XRD data (Fig. 2g) and (ii) by its light brown and gray coloration (Fig. 2a). That is because copper oxidation into Cu₂O is spontaneous at room temperature and its oxidation into CuO initiates at temperatures above 250 °C at atmospheric pressures [59] (see Supplementary Figure S3), which was also confirmed by Rodriguez et al., [39] and, thus, CuO is only present in HT-ER samples whose T_{max} are 325 – 399 °C. Besides oxygen content, the temperature increase can induce thermal coarsening which is investigated as a function of the powder layer thickness via BET and BJH methods. Although PCu powders that do not experience HT-ER have T_{max} ranging from 29 to 58 °C which is below PSST, [37] BJH and BET data revealed (Fig. 2i, j) that the average pore size increases and specific surface area decreases with increasing mass and T_{max}, respectively (Fig. 2j), which is indicative of thermal coarsening. [60,61] This apparent contradiction might be explained by the temperature difference between the top surface of the powder pack from where the IR thermometer measurement is taken and its core, suggesting its core might experience temperatures higher than 95 °C. Note that thermal coarsening rates might become limited as the oxide layer becomes thicker and inhibits surface diffusion. [62] For samples that experience HT-ER, surface area continues to decay with increasing mass and T_{max} (Fig. 2i). However, a sharp drop in their pore size is observed which is consistent with SEM image analysis (Fig. 2d, e). This result is expected since HT-ER powders are mostly oxidized and simultaneously experience high temperatures leading to their expansion due to oxygen incorporation and their bulk sintering [63] resulting in shrinkage, both of which serve to reduce porosity. The data collected in this experiment is summarized in Supplementary Table S4.

2.2. Nanoscale welding of nanoporous copper powders

With the goal of establishing welding across nanoporous copper powders to form electrically conductive parts as potential high-surface area electrodes for energy applications, it was necessary to investigate (i) the thermal reduction of oxides during sintering in 95% Ar/5% $\rm H_2$ mixture, (ii) welding of copper across powder-to-powder interfaces and (iii) their electrical resistance as a function of sintering temperature. Unlike traditional sintering approaches that take place at 70-92% of

the melting point of a material to weld powders (i.e., $750-1000\,^{\circ}\text{C}$ for copper), the central hypothesis is that individual ligaments can be welded across their powder-to-powder interface by surface diffusion and driven by the metastability of the nanoporous copper and the mismatch in surface energy upon contact between ligaments at temperatures as slow as 28-46% of the melting temperature of Cu (i.e., $300-500\,^{\circ}\text{C}$). Such low temperatures not only serve to establish welding and the formation of a rigid and conductive solid, but also to preserve the nanoscale porosity and high-surface area of the nanoporous copper which is not stable at high temperatures (i.e., $600-700\,^{\circ}\text{C}$). [64]

To address this hypothesis, this paper first examined the oxide decomposition as a necessary step towards nanoscale metal welding. The resistance across a powder pack during heating from room temperature to 400 $^{\circ}\text{C}$ in a reducing atmosphere (Ar mixed with 5 vol.% of

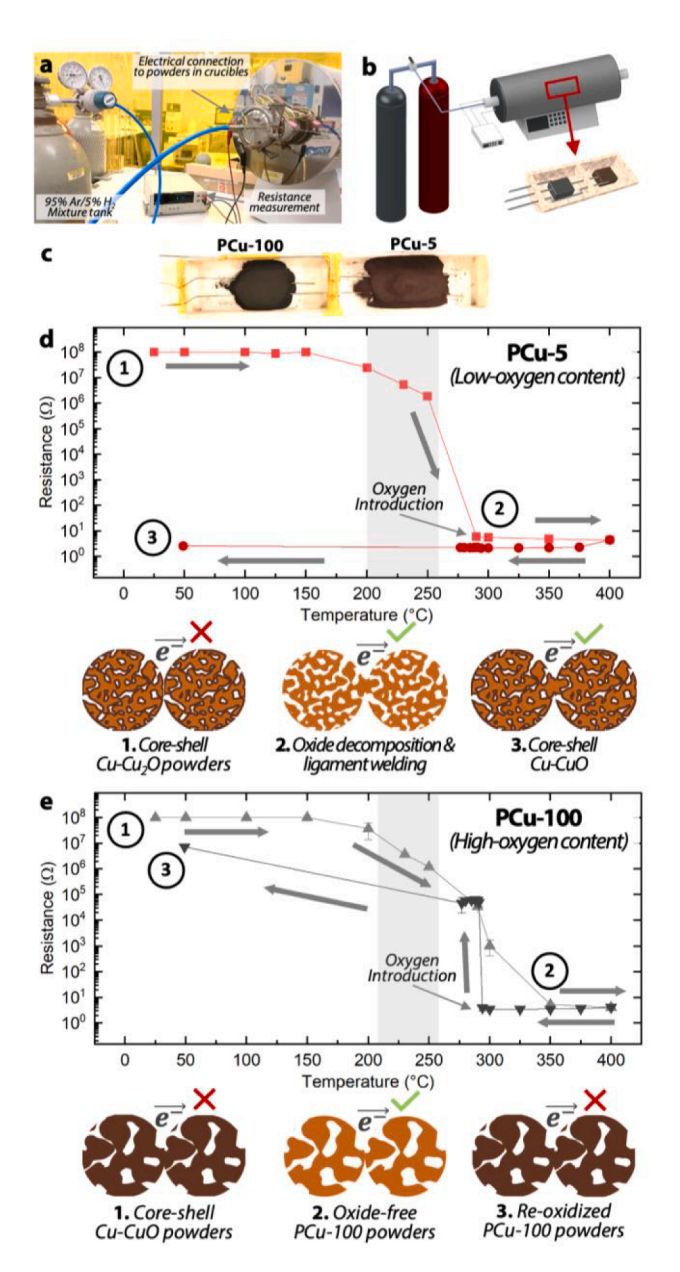


Fig. 3. (a) The setup for in-situ resistance measurements during heating in reducing atmosphere (Ar/ $\rm H_2$) of compacted powders and (b) its illustration showing wiring connections outside and inside the furnace, and (c) loaded PCu-100 and PCu-5 samples onto crucible and wiring. Resistance measurements for (d) PCu-5 and (e) PCu-100 with schematics highlighting nanoscale welding at PCu powder interface and its surface oxide state, as well as electrical conductivity when present.

H₂) was monitored in-situ as illustrated in Fig. 3a-c. At room temperature, powders possess a high resistance due to the presence of the oxide (see #1 in Fig. 3d, e). An 8-order of magnitude drop in resistance occurs for both PCu-5 and PCu-100 at the onset temperature of $\sim 200~^{\circ}\text{C}$ which indicates that Cu₂O and CuO were thermally reduced in reducing atmospheres which agrees with prior literature. [39] Oxide reduction has an onset at $\sim 200~^{\circ}\text{C}$ for both samples and ends at $\sim 270~^{\circ}\text{C}$ and $\sim 350~^{\circ}\text{C}$ for PCu-5 and PCu-100 respectively (see #2 in Fig. 3d, e). After that, powders are allowed to sinter in its oxide-free state. During the cooling cycle, oxygen is introduced at 300 °C to intentionally passivate the welded powders with an oxide. If ligaments weld during heating, that step will passivate them, ligaments will be 'bridged' between powders and electrical contact will be maintained (see schematics in Fig. 3d,e) which was indeed the case for the PCu-5 sample (see #3 in Fig. 3d). However, the PCu-100 sample exhibited a 7-order of magnitude gain in its resistance during the cooling cycle (see #3 in Fig. 3e) which indicates the breakage of electrical contact between particles. Also, the PCu-5 sample appears solid at the end of the cooling cycle while the PCu-100 sample is still in a powder consistency and cannot hold its shape. The lack of ligament-like morphology in the PCu-100 sample is the primary cause for its poor sinterability and limited nanoscale welding. Additional evidence related to this point is discussed in Supplementary Section S2.

2.3. Powder casting of porous copper parts

Since the approach to synthesize PCu powders in this paper allows them to preserve their spherical shape after dealloying and, albeit shrinkage of its diameter (e.g., 11% by volume) is expected (see Supplementary Section 3), their flowability which was measured by the Carney method which yielded a flow rate of 32.9 s per 50 g for PCu while its solid CuAl precursor failed the same test after 3 taps (see

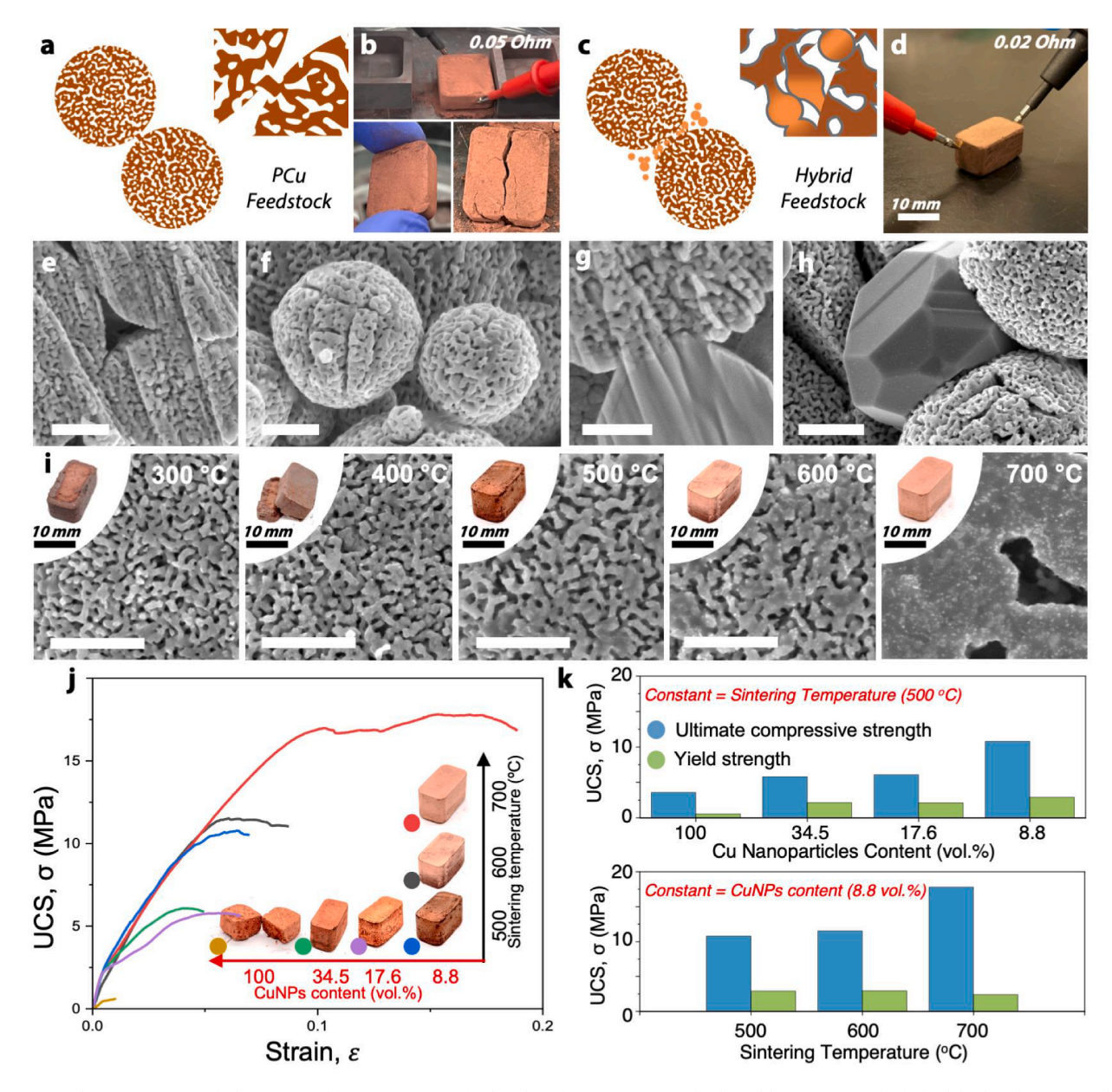


Fig. 4. (a, c) Schematics of a single ligament welding in pure PCu feedstock and formation of multiple welding points in the hybrid feedstock respectively. Photographs of sintered copper block using (b) PCu powders and (d) hybrid feedstock, both demonstrating low electrical resistance. FIB and SEM images demonstrating welding neck between (e, f) PCu powders. (g, h) PCu and CuNPs. (i) SEM images of ligaments in sintered blocks (insets show a corresponding block). (j) Stress-strain curves. (k) Summarized results on mechanical testing as a function of sintering temperature and CuNPs content. Scale bar is 500 nm unless otherwise indicated.

Supplementary Video S9 and Supplementary table S5 for additional details). This value is comparable s comparable to that of metal gas atomized spherical powders with similar densities [65] suggesting that applications in powder casting and additive manufacturing are possible. In a first attempt, pure PCu-5 powder was sintered in an open-die mold at high-temperatures (600 – 700 °C) in reducing atmosphere (i.e., 95% Ar/5% H₂ mixture) and resulted into a conductive solid with poor mechanical integrity and brittleness evidenced by its fracture upon the soft touch of hand manipulation (Fig. 4b) and loose aggregates (i.e., crumbly). The low electrical resistance (Fig. 4b) and rigidity of the part established after sintering and exposure to atmosphere is attributed to nanoscale welding of ligaments in PCu bridging the metal across particle-to-particle interfaces since any contact or welding between Cu₂O would not yield a conductive solid. In fact, FIB cross-sections and SEM images of the contact interface between sintered PCu powders confirm this hypothesis (Fig. 4e, f) and no oxygen is observed inside the welded interface according to EDS measurements (Supplementary Figure S7). The brittle behavior is attributed to the low-density of contact points between powders which arises from the size difference between the ligament size and the powder size which is greater than an order of magnitude. Note that thermal coarsening of the nanoporous structure increases the ligament size relative to the powder size and may promote necking formation. In a second attempt, this issue was addressed by using a hybrid feedstock in which CuNPs [66] are added in small fractions (i.e., 8.8 - 34.5 vol.% of CuNPs) to promote welding between themselves and P-Cu powders (Fig. 4c) and increase the neck size between PCu particles. Note that loading of CuNPs by volume was calculated considering skeletal density and shrinkage of PCu powder after dealloying (see Supplementary Section S3) and neglects density changes due to oxidation.

First, casted blocks with 8.8 vol.% of CuNPs using this hybrid feedstock were sintered at 300 – $700\,^{\circ}\text{C}$ and did not crumble apart or crack upon soft touch with shape retention after demolding (Fig. 4d; see Supplementary video) which is attributed to additional nanoscale welding between PCu and CuNPs (Fig. 4g, h). Due to Ostwald ripening, [45,67] CuNP agglomerates coalesce between themselves, and recrystallize at 400 °C and above, leading to crystal growth and faceting (Fig. 4h; Supplementary Figure S4) which resembles literature on copper electronic inks. [40] At the same time, CuNPs weld with ligaments on the surface of PCu powder. However, it is hard to pinpoint the cause for the crystallite size of sintered CuNP agglomerates ($\sim 1-5 \,\mu m$ in size) to be much larger than ligaments in PCu which remain small ($\sim 24 - 36$ nm) even after heat treatment at 600 °C (see Supplementary Figure S1), suggesting the latter is more stable than the former. This is a key phenomenon in sintering of hybrid feedstocks that enables the preservation of the high-surface area of PCu while improving the neck size between PCu powders. To explain it, three possible reasons are: (i) diffusion of impurity species (see Supplementary Section 5) across the interface between PCu and CuNPs which might lower the energy barrier for recrystallization of CuNPs at 400 °C, (ii) CuNPs might be expanding due to their coefficient of thermal expansion (CTE) while in the mold and, thus, under compressive stress which promotes Ostwald ripening albeit some reports on literature cite nanoporous metals to have a negative CTE due coarsening [68,69] - and (iii) the hyperbolic paraboloid shape (e.g., 'horse saddle' shape) of ligaments in PCu with both negative and positive curvatures yields a higher activation energy for thermal coarsening than that of the recrystallization of spherical CuNPs by Ostwald ripening. Lastly, another observation is that the recrystallization front of CuNP conformed to the surface of PCu powders which effectively closes its surface pores in PCu into a thermodynamically stable configuration (e.g., closed round pore) at their interface (Fig. 4g, h).

While parts are solid and oxygen-free after sintering inside the Ar glovebox, heating was observed upon their removal to air in ambient conditions. Similar to drying of the PCu feedstock at different powder thicknesses (Fig. 2), parts heated to its T_{max} and formed copper oxides on

its surface. Parts sintered at 300 and 400 $^{\circ}\text{C}$ exhibited $T_{max} > 365 \,^{\circ}\text{C}$ and lost its structural integrity (i.e., cracked in half) with its outer shell heavily oxidized to CuO evidenced by the change in color on its outer layer (see inset photograph in Fig. 4i). Therefore, it is recommended for these parts to be used in inert environment only or in a packaged device. Parts sintered at 500, 600 and 700 $^{\circ}$ C did not overheat ($T_{max} < 102 \,^{\circ}$ C) upon their exposure to air in comparison to the parts sintered at 300 and 400 °C which is attributed to the thermal coarsening of its ligaments (Fig. 4i) and reduction in surface area which minimizes heat generation during its exposure to the atmosphere. The derived slope of ligament coarsening (i.e., $nE_a = 0.02$) (see Supplementary Figure S1) is much lower than prior literature [70,71] which is counterintuitive since the surface of the PCu is free from oxygen due to its reduction with hydrogen and, therefore, the diffusion of copper atoms should not be limited. Note that small segments (i.e., < 1 mm) were extracted from 300 to 400 °C samples to eliminate heat generation in the sample and to analyze ligament diameter and extract nEa, and that the ligament morphology disappears on the PCu surface at 700 °C (see Fig. 4i). It is possible that the residual aluminum (~ 0.9 at.%) present in the samples prior to sintering is not dissolved in the copper matrix as expected from its phase diagram since dealloying and surface passivation occur near room temperature. Thus, it is possible for this observation to be attributed to melting of CuAl phases that are reminiscent in PCu powder. In fact, DSC and TGA data of PCu-5 powder show the onset of an endothermic peak at 650 °C without any loss of its mass suggesting it is melting (see Supplementary Figure S2). The thermal stability of PCu up to 600 °C observed in casted parts (Fig. 4i) can be beneficial for attaining the lowest possible shrinkage of the final product (since thermal coarsening leads to its shrinkage and negative CTE). In fact, it was found that sintered Cu blocks sintered at 600 °C result in 9.2, 20.7 and 29.7 vol.% shrinkage at 8.8, 17.6 and 34.5 vol.% of CuNPs loading, respectively, (see Supplementary Figure S5) which allows for the conclusion that the CuNP is the main contributor to shrinkage at high loadings. An increase in shrinkage with increase in CuNPs content can be explained by (i) their low thermodynamic stability which leads to Ostwald ripening and the coalescence of nanoparticles into solid micron-sized crystallites and (ii) low packing factor of CuNPs in the mold due to their low flowability.

To quantify the mechanical performance of sintered Cu blocks, compression tests were performed on the samples sintered from 500 to 700 °C which excludes the ones not stable in air (i.e., T = 300 - 400 °C). First, samples sintered at 500 °C with increasing CuNP loading exhibit a decreasing trend in the ultimate compression strength (UCS) (Fig. 4k). At high CuNPs loadings, rather than filling the gaps between the necks of welded PCu powders, sintered CuNP can fill the region between PCu powders and eliminate weld regions between them. Since they are expected to form low packing density due to its poor flowability characteristics, the resulting UCS is lower. Note that the solid cross-sectional area used to calculate the stress and UCS values are obtained using the exterior dimensions of the block and accounting for its internal porosity and reduction in solid cross-section area as demonstrated in the Supplementary Section 4. Second, by maintaining the CuNPs loading constant (i.e., 8.8 vol.%), an increasing trend in the UCS with increasing temperature is observed which highlights its trade-off with the final pore size and surface area since the latter is also temperature dependent. The UCS values yielded 3.6 MPa (i.e., for pure CuNPs sintered at 500 $^{\circ}\text{C})$ and 17.8 MPa (i.e., for PCu with 8.8 vol.% of CuNPs sintered at 700 $^{\circ}$ C) and the latter is still one order of magnitude less than bulk copper. As a reference, the sintered block made of pure CuNPs exhibited even lower UCS of 3.6 MPa which, albeit measurable, sintered CuNPs appears to be crumbly. This can be explained by their poor packing in the mold due to its poor flowability. All sintered parts independent of both sintering temperature and CuNPs content yielded at 2.4 \pm 0.3 MPa which is indicative of the presence of defects in the sintered Cu parts that fracture at stress concentrations around the neck zones whose cross-sectional area are still too small compared to the powders size. Note that strengthening mechanisms associated with nanoporous metals (i.e.,

Gibson-Ashby) [72] are not expected to play a role in it. In context with studies of mechanical properties of porous copper and its composites, Jiang et al. [43] achieved ultimate tensile strength as high as 260 MPa for porous Ni nanolattices which is attributed to their low defect density, however, the processing throughput of its manufacturing methods are expected to be prohibitive given the high-volume production required for the proposed energy applications. Wang et al. [38] demonstrated high values of UCS (i.e., > 50 MPa) and high relative density of 0.29 – 0.98 for PCu parts fabricated by spark plasma sintering (SPS) at pressure range of 2.5 - 20 MPa respectively, however, ligament sizes that are an order of magnitude higher (i.e., 480 nm) than those attained in this study and SPS is not compatible with 3D printed parts as this die-compaction process often results in densification inhomogeneity due to thickness difference in the sample. [73] Therefore, the low values of UCS in this paper is the trade-off for (i) the scalability of the approach herein developed, (ii) ligament sizes and surface area of electrode, and (iii) 3D manufacturability of the final part. A summary of the mechanical testing data is presented below in Table 1.

2.4. Conclusion

In this study, a protocol for large scale (i.e., > 25 g/h) production of a novel hybrid feedstock containing porous Cu micron-sized spherical powder and Cu nanoparticles with 8.8 - 34.5 vol.% of the latter was developed to fabricate load bearing and electrically conductive electrodes via open-die powder casting, and a trade-off between its strength and high-surface area at elevated sintering temperatures was demonstrated. It was possible to achieve high throughput production of precipitate-free porous Cu powder from Cu-Al gas atomized precursors due to (i) its high-surface area compared to other bulk precursors leading to high dealloying rates, (ii) dealloying in excessive amount of highly concentrated (i.e., 3 M NaOH) solution to stabilize the pH during the etching process and (iii) by titrating powder (i.e., 1 g/30 s) into solution to prevent excessive hydrogen gas generation, aluminum buildup in the etching bath and suppress thermal runaway. In terms of scalability of the synthesis process, it is worth nothing that reagent grade NaOH is expensive and alternative solutions might include cost scaling in large orders, new alkaline chemistries and the use of less pure grades of NaOH. [74] It was found that the drying of powder after dealloying is a step accountable for oxygen incorporation into porous Cu powder. XRD analysis revealed that, as a function of temperatures after the exposure, either (i) Cu₂O containing core-shell porous Cu structure can be formed (i.e., PCu-5) or (ii) crystalline Cu can be completely converted to CuO with substantial thickening of ligaments (i.e., PCu-100). Alternative strategies to decrease the final oxygen content in the PCu powders may include: (i) atomic layer deposition (ALD) and chemical vapor deposition (CVD) of carbides, [55] nitrides [56] and alumina [57] oxygen-barrier passivation layers, (ii) surface area reduction via thermal coarsening in vacuum [58] before exposure to atmosphere, and (iii) its transfer to an inert atmosphere for further processing. The hybrid feedstock containing PCu-5 powder and CuNPs was produced via planetary mixing and casted in the open-die mold in hydrogen containing atmosphere at temperatures from 300 to 700 $^{\circ}$ C to fabricate electrically conductive parts while preserving nanoporosity due to thermal stability of PCu. After compression testing it was found that, although the parts are mechanically stable, they exhibit low values in ultimate compression strength compared to existing studies owning to their intra-particle porosity and limited necking formation. Nevertheless, this work suggests the use of the developed hybrid feedstock in powder metallurgy processes such as powder injection molding and additive manufacturing techniques which can in the future fabricate large-scale 3D hierarchical load bearing electrodes with high surface area.

2.5. Methods

Spherical Copper-Aluminum (Cu $_{33}$ Al $_{67}$ in atomic fractions) gas atomized powders were purchased from Valimet Inc. Corresponding particle size distribution of Cu $_{33}$ Al $_{67}$ powders according to Aerodynamic particle sizer (APS) measurements performed by Valimet Inc. was as following: D $_{10}$ – 4.36 um, D $_{50}$ – 11.76 um, D $_{90}$ – 28.55 um. 37 wt.% Sodium hydroxide (Reagent grade) was purchased from Sigma Aldrich. Anhydrous ethanol (Reagent grade) was purchased from Carolina. Automatic self-zeroing burette (10 ml) with a 1000 ml glass vessel was purchased from Eisco Labs.

In this study, PCu powder was fabricated using two different approaches: (1) by titrating 260 ml of concentrated NaOH solution at a titration rate of 4 ml/min using 10 ml self-zeroing burette into DI water (2240 ml) with a dispersed CuAl precursor powder (50 g), and (2) by titrating CuAl precursor powder (50 g) at a rate of 1 g every 30 s into 3 M NaOH solution (2500 ml).

In the first approach, 5000 ml glass beaker containing 2240 ml DI water with a dispersed CuAl powder was placed on a hotplate with a setpoint temperature of 250 $^{\circ}\text{C}$ and heated to 50 $^{\circ}\text{C}$ within 30 min at a constant stirring rate of 300 RPM. Immediately after reaching the target temperature, the hotplate was turned off and NaOH solution was titrated using a burette at a rate of 8 ml/min resulting in 32 min 30 s of total dealloying time. The hydrogen bubbles were generated as a result of aluminum etching and were evidenced throughout the whole dealloying process which is an indicator of slow etching reaction rate.

In the second approach, 5000 ml glass beaker containing 2500 ml of freshly prepared 3 M NaOH solution was placed on a hotplate. Due to the exothermic reaction of NaOH dissolution with water, the prepared solution naturally heated to $52\pm1\,^{\circ}\text{C}$. The beaker with solution was left on a hotplate to cool down to 45 $^{\circ}\text{C}$ with a stirring speed of 300 RPM and immediately after that the temperature on a hotplate was set to 250 $^{\circ}\text{C}$ and solution was heated to 50 $^{\circ}\text{C}$. After reaching the desired temperature, CuAl powder was titrated at a rate of 1 g every 30 s with a total titration time of 24 min 30 s. After all powder was used, PCu was kept 5 additional minutes in dealloying bath to complete Al etching. The hydrogen bubbles were rapidly generated and were observed in first 5 min of dealloying indicating that the rate of the aluminum etching reaction is higher than using first titration approach.

The temperature profiles were recorded for PCu fabrication using both titration approaches from the start of titration and until produced

Table 1

The data and observations of PCu blocks sintered at temperatures from 300 to 700 °C. Note that the term 'crumbly' refers to samples that fractured upon hand manipulation and 'solid' refers to samples that were submitted for mechanical compression testing.

Sintering temperature, (°C)	CuNPs content (vol.%)	T _{max} (°C)	Structural integrity (in Ar)	Structural integrity (in air)	Estimated YCS (MPa)	Measured aUCS (MPa)	Estimated UCS (MPa)
300	8.8	380	Solid*	Crumbly*	Not tested	Not tested	Not tested
400	8.8	365	Solid	Crumbly	Not tested	Not tested	Not tested
500	34.5	102	Solid	Solid	2.1	1.6	5.8
500	17.6	42	Solid	Solid	2.1	1.7	6.1
500	8.8	54	Solid	Solid	2.9	2.2	8.8
500	100	24	Crumbly	Crumbly	0.5	1.6	3.6
600	8.8	56	Solid	Solid	2.9	2.3	11.5
700	8.8	27	Solid	Solid	2.4	3.6	17.8

powder was ready for washing. PCu powder was washed with 1 L of DI water and 200 ml of anhydrous ethanol. Powders were transferred to the vacuum oven in one beaker to dry at 90 $^{\circ}$ C for 4 h. Note that drying procedure was changed in the case of the oxide incorporation study since it was found that drying of powder in large amounts with low surface-to-volume ratio can lead to exothermic runaway with rapid heat generation. A detailed drying protocol is discussed below.

2.5.1. PCu powder drying for the oxide incorporation study

The nature of oxide incorporation in PCu powders fabricated using the 2nd approach was studied as follows. In the first experiment, a freshly prepared PCu powder with a mass total of 25 g (PCu-25) were dried in vacuum oven at 90 °C for 8 h and exposed to air in the same beaker with a high-aspect ratio (i.e., 130 and 85 mm in height and width respectively) and the oxidation temperature and $T_{\rm max}$ were recorded. Then, the aspect ratio of the beaker was decreased (i.e., 18 and 145 mm in height and width respectively) and the same quantity of PCu powder (i.e., 25 g) was dried and exposed to air. In the second experiment, the low-aspect ratio beaker was used as a vessel for PCu powder drying and the quantity of the powder was varied from 5 to 100 g per beaker (i.e., when the thickness of powder layer is from 0.3 to 6 mm). The temperatures were recorded by IR thermocouple.

SEM and EDS analysis of PCu powders was performed using Zeiss Auriga SEM. XRD analysis was performed on Bruked D8. BET specific surface area and BJH average pore size were analyzed on Micromeritics Tristar II Plus equipment. The sintering of powder was performed in Ar and 95% Ar/5% $\rm H_2$ mixture environments in Carbolite Gero EST1200 tube furnace. The drying of PCu powder was performed in vacuum oven (Across International. The handling of PCu powder was performed both in air and in Ar-filled glovebox.

2.5.2. Flowability test

Flowability was evaluated with Hall and Carney flowmeters indicated by ASTM B213–20 and ASTM B964–16 standard tests, respectively. In both tests, a weighted mass of 50 g of dry powders was deposited into the flowmeter funnel with blocked discharge orifice and once discharge orifice was released, flow rate was timed as the metric of flowability. Hence, the shorter the time the more flowable the powders are. Standards regulate that if powders are not flowable through the initially used Hall flowmeter funnel (diameter of discharge orifice $\emptyset = 0.10$ in), then tests are to be performed with Carney flowmeter funnel (diameter of discharge orifice $\emptyset = 0.20$ in). The process was repeated 3 times for each sample and both Hall and Carney flowmeter funnels were obtained from Qualtech Products Ltd.

2.5.3. Sintering of PCu powder parts

In the first sintering experiment, PCu-5 powder was sintered in 95% Ar/5% H_2 mixture atmosphere at 700 $^{\circ}$ C in a graphite crucible for 24 h. In the second experiment, PCu-5 powder was homogenized with 300 nm CuNPs (8.8 – 34.5 vol.%) using ball mixing machine operated without milling balls and at low attrition speeds effectively acting as a planetary mixer. It is not expected that this step introduces any morphological changes to the microstructure of the feedstock. The sintering was performed at temperatures from 300 to 700 $^{\circ}$ C. After sintering, casted parts were removed from inert atmosphere to air. Mechanical testing of casted parts was performed on Instron 59,944 with 1 kN of applied force.

2.5.4. Nanoscale welding of nanoporous copper powders

Configuration for in-situ resistance measurements consisted in the use of ER316L wires as connection probes to the samples in alumina crucibles under 95% Ar/5% $\rm H_2$ mixture and oxygen atmospheres. The experiment was conducted with temperatures up to 400 $^{\circ}\text{C}$, at 5 $^{\circ}\text{C/min}$ with three resistance measurements taken for each sample every 50 $^{\circ}\text{C}$ step during heating cycle.

2.5.5. Analysis of materials with differential scanning calorimetry

Porous copper powders and copper nanoparticles were analyzed using Differential Scanning Calorimetry (DSC) and Thermogravimetric (TGA) techniques on SETARAM LABSYS evo DTA/DSC. Samples were loaded in 20-50 mg quantities into alumina crucible and analyzed against alumina particles. At first, helium gas was purged for 20 min to avoid any buoyancy effects at higher temperatures. After that, samples were heated at 5 K/min until 1100 °C is reached.

Data availability

The raw data required to reproduce these findings are available to download from supplementary files. The processed data required to reproduce these findings are available to download from supplementary files.

Author contributions

S.N. and B.A. conceived research. S.N., N.K. and B.A. designed research. S.N., N.K., E.D. and B.A. performed research. All the authors discussed the results and commented on the manuscript.

CRediT authorship contribution statement

Stanislau Niauzorau: Methodology, Investigation, Data curation, Writing – original draft, Conceptualization, Visualization, Formal analysis. Natalya Kublik: Methodology, Investigation, Data curation, Conceptualization, Visualization, Writing – review & editing. Emmanuel Dasinor: Methodology, Data curation. Amm Hasib: Methodology. Aliaksandr Sharstniou: Methodology. Bruno Azeredo: Writing – review & editing, Conceptualization, Supervision, Project administration, Funding acquisition.

Declaration of Competing Interest

The authors declare that they have no known competing financial interests or personal relationships that could have appeared to influence the work reported in this paper.

The authors declare the following financial interests/personal relationships which may be considered as potential competing interests:

Dr. Bruno Azeredo owns interest in a start-up company named Nanobionics that does not operate in any area related to this publication.

Data availability

Data will be made available on request.

Acknowledgments

We acknowledge the use of facilities with the LeRoy Eyring Center for Solid State Science at Arizona State University and John M. Cowley High Resolution Electron Microscopy at Arizona State University. The authors acknowledge also financial support from the NSF CMMI Grants No. 1932899 (S.N., N.K., and B.A.).

Supplementary materials

Supplementary material associated with this article can be found, in the online version, at doi:10.1016/j.apmt.2023.101802.

References

- A. Chuang, J. Erlebacher, Materials (Basel) 13 (2020) 3706.
 C. Zhu, Z. Qi, V.A. Beck, M. Luneau, J. Lattimer, W. Chen, M.A. Worsley, J. Ye, E.
- B. Duoss, C.M. Spadaccini, C.M. Friend, J. Biener, Sci. Adv. 4 (2018) 9459.
- [3] P. Zhu, Z. Wu, Y. Zhao, Scr. Mater. 172 (2019) 119.

- [4] Z. Wang, P. Liu, J. Han, C. Cheng, S. Ning, A. Hirata, T. Fujita, M. Chen, Nat. Commun. 8 (2017) 1066.
- [5] J. Li, W. Fu, B. Zhang, G. Zhu, N. Miljkovic, ACS Nano 13 (2019) 14080.
- [6] J.H. Pikul, J. Liu, P. v Braun, W.P. King, J. Power Sources 315 (2016) 308.
- [7] Y. Lu, J.Y. Huang, C. Wang, S. Sun, J. Lou, Nat. Nanotechnol. 5 (2010) 218.
- [8] M. Hakamada, M. Mabuchi, J. Mater. Res. 24 (2009) 301.
- [9] H. Aihara, J. Zider, G. Fanton, T. Duerig, Int. J. Biomater. 2019 (2019), 4307461.
- [10] A. Maznoy, A. Kirdyashkin, V. Kitler, A. Solovyev, J. Alloys Compd. 697 (2017) 114.
- [11] B.25emC. Tappan, S.25emA. Steiner, E.25emP. Luther, Angewandte Chemie Int. Ed. 49 (2010) 4544.
- [12] S.K. Saha, C. Divin, J.A. Cuadra, R.M. Panas, J. Micro Nanomanuf. 5 (2017), 031002.
- [13] K.W. Tan, U. Wiesner, Macromolecules 52 (2019) 395.
- [14] E. Cara, F.F. Lupi, M. Fretto, N. de Leo, M. Tortello, R. Gonnelli, K. Sparnacci, L. Boarino, Nanomaterials 10 (2020) 280.
- [15] H. Zhang, P.v. Braun, Nano Lett. 12 (2012) 2778.
- [16] A.B.D. Nandiyanto, T. Ogi, W.-.N. Wang, L. Gradon, K. Okuyama, Adv. Powder Technol. 30 (2019) 2908.
- [17] T. Song, M. Yan, M. Qian, Corros. Sci. 134 (2018) 78.
- [18] K. Zhang, X. Tan, J. Zhang, W. Wu, Y. Tang, RSC Adv. 4 (2014) 7196.
- [19] Z. Qi, M.M. Biener, A.R. Kashi, S. Hunegnaw, A. Leung, S. Ma, Z. Huo, K.P. Kuhl, J. Biener, J. CO2 Utilizat. 45 (2021), 101454.
- [20] Y. Sun, Y. Ren, Vacuum 122 (2015) 215.
- [21] J.S. Corsi, J. Fu, Z. Wang, T. Lee, A.K. Ng, E. Detsi, ACS Sustain. Chem. Eng. 7 (2019) 11194.
- [22] Z. Dan, J. Qu, Y. Yang, F. Qin, H. Chang, Nanomaterials 8 (2018) 581.
- [23] L. Gu, S. Wang, X. Hui, F. Li, H. Lin, K. Wu, Nanotechnology 33 (2022), 135713.
- [24] I. McCue, A. Karma, J. Erlebacher, MRS Bull. 43 (2018) 27.
- [25] A.V. Okulov, S.-.H. Joo, H.S. Kim, H. Kato, I.V. Okulov, Metals (Basel) 10 (2020) 1396.
- [26] I. McCue, E. Benn, B. Gaskey, J. Erlebacher, Annu. Rev. Mater. Res. 46 (2016) 263.
- [27] S. Niauzorau, A. Sharstniou, V.K. Sampath, N. Kublik, H. Bandarenka, B. Azeredo, ACS Appl. Mater. Interfaces 14 (2022) 17927.
- [28] H. Hui, R. Xia, J. Li, Q. Mei, Y. Ma, F. Chen, Y. Lei, Nanomaterials 8 (2018) 540.
- [29] C. Rurainsky, A.G. Manjón, F. Hiege, Y.-.T. Chen, C. Scheu, K. Tschulik, J. Mater. Chem. A Mater. 8 (2020) 19405.
- [30] Y.K. Chen-Wiegart, S. Wang, W.-.K. Lee, I. McNulty, P.W. Voorhees, D.C. Dunand, Acta Mater. 61 (2013) 1118.
- [31] S. Kitabayashi, M. Nakano, K. Nishikawa, N. Koga, J. Chem. Educ. 93 (2016) 1261.
- [32] H. Zhang, X. Zhang, T.R. Graham, C.I. Pearce, H. Hlushko, J.A. LaVerne, L. Liu, S. Wang, S. Zheng, Y. Zhang, S.B. Clark, P. Li, Z. Wang, K.M. Rosso, Inorg. Chem. 60 (2021) 9820.
- [33] A. Chuang, J. Baris, C. Ott, I. McCue, J. Erlebacher, Acta Mater. 238 (2022), 118213.
- [34] D. Bell, D. Rall, M. Großeheide, L. Marx, L. Hülsdünker, M. Wessling, Electrochem. Commun. 111 (2020), 106645.
- [35] S. Wang, L. Liu, J. Hazard. Mater. 340 (2017) 445.
- [36] Y. Sun, T.J. Balk, Scr. Mater. 58 (2008) 727.
- [37] R. Ramesh, S. Niauzorau, V.K. Sampath, L. Wang, B.P. Azeredo, Adv. Opt. Mater. 10 (2022), 2102479.
- [38] L. Wang, H. Xie, J.-.C. Shao, H. Yang, P.-.Z. Feng, H.-.J. Jin, Scr. Mater. 203 (2021), 114114.
- [39] J.Y. Kim, J.A. Rodriguez, J.C. Hanson, A.I. Frenkel, P.L. Lee, J. Am. Chem. Soc. 125 (2003) 10684.

- [40] H.-.J. Hwang, K.-.H. Oh, H.-.S. Kim, Sci. Rep. 6 (2016).
- [41] C. Cai, S. Guo, B. Li, Y. Tian, J.C.D. Qiu, C.-N. Sun, C. Yan, H.J. Qi, K. Zhou, ACS Appl. Mater. Interfaces 13 (2021) 48709.
- [42] C. Yang, C. Zhang, L. Liu, J. Mater. Chem. A Mater. 6 (2018) 20992.
- [43] Z. Jiang, J.H. Pikul, Nat. Mater. 20 (2021) 1512.
- [44] J. Ahn, S. Hong, Y.-.S. Shim, J. Park, Appl. Sci. 10 (2020) 8780.
- [45] T.W. Hansen, A.T. DeLaRiva, S.R. Challa, A.K. Datye, Acc. Chem. Res. 46 (2013) 1720.
- [46] S.S. Welborn, A. Simafranca, Z. Wang, H. Wei, E. Detsi, Scr. Mater. 200 (2021), 113901.
- [47] Z. Wang, L. Wang, C. Qin, J. Liu, Y. Li, W. Zhao, Mater. Res. 17 (2014) 1003.
- [48] T. Lee, J. Fu, V. Basile, J.S. Corsi, Z. Wang, E. Detsi, Renew. Energy 155 (2020)
- [49] W. Liu, L. Chen, X. Dong, J. Yan, N. Li, S. Shi, S. Zhang, Sci. Rep. 6 (2016) 36084.
- [50] T. Kou, C. Jin, C. Zhang, J. Sun, Z. Zhang, RSC Adv. 2 (2012) 12636.
- [51] Y.K. Chen-Wiegart, S. Wang, Y.S. Chu, W. Liu, I. McNulty, P.W. Voorhees, D. C. Dunand, Acta Mater. 60 (2012) 4972.
- [52] N. Wang, Y. Pan, S. Wu, J. Mater. Sci. Technol. 34 (2018) 1162.
- [53] J.A. van Orman, K.L. Crispin, Rev. Mineral. Geochem. 72 (2010) 757.
- [54] W. Hu, F. Donat, S.A. Scott, J.S. Dennis, RSC Adv. 6 (2016), 113016.
- [55] D.S. Gardner, C.W. Holzwarth, Y. Liu, S.B. Clendenning, W. Jin, B.-.K. Moon, C. Pint, Z. Chen, E.C. Hannah, C. Chen, C. Wang, E. Mäkilä, R. Chen, T. Aldridge, J. L. Gustafson, Nano Energy 25 (2016) 68.
- [56] A. Shahravan, T. Desai, T. Matsoukas, ACS Appl. Mater. Interfaces 6 (2014) 7942.
- [57] L. Qian, B. Das, ECS Trans. 33 (2010) 3.
- [58] A.Y. Chen, S.S. Shi, F. Liu, Y. Wang, X. Li, J.F. Gu, X.F. Xie, Appl. Surf. Sci. 355 (2015) 133.
- [59] G. Honjo, J Phys.l Soc Japan 4 (1949) 330.
- [60] H. Jeon, N.-.R. Kang, E.-.J. Gwak, J. Jang, H.N. Han, J.Y. Hwang, S. Lee, J.-.Y. Kim, Scr. Mater. 137 (2017) 46.
- [61] J. Gubicza, P. Jenei, G. Han, P.-T. Hung, Y. Song, D. Park, Á. Szabó, C. Kádár, J.-H. Kim, H. Choe, Materials (Basel) 14 (2021) 2691.
- [62] A. Kosinova, D. Wang, E. Baradács, B. Parditka, T. Kups, L. Klinger, Z. Erdélyi, P. Schaaf, E. Rabkin, Acta Mater. 127 (2017) 108.
- [63] H. Vu, D. Nguyen, J.G. Fisher, W.-H. Moon, S. Bae, H.-G. Park, B.-G. Park, J. Asian Ceramic Societies 1 (2013) 170.
- [64] R.N. Viswanath, V.A. Chirayath, R. Rajaraman, G. Amarendra, C.S. Sundar, Appl. Phys. Lett. 102 (2013), 253101.
- [65] L.J. Jallo, M. Schoenitz, E.L. Dreizin, R.N. Dave, C.E. Johnson, Powder Technol. 204 (2010) 63.
- [66] D. Deng, Y. Jin, Y. Cheng, T. Qi, F. Xiao, ACS Appl. Mater. Interfaces 5 (2013) 3839.
- [67] M.B. Gawande, A. Goswami, F.-.X. Felpin, T. Asefa, X. Huang, R. Silva, X. Zou, R. Zboril, R.S. Varma, Chem. Rev. 116 (2016) 3722.
- [68] A. Saboori, S. Moheimani, M. Pavese, C. Badini, P. Fino, Metals (Basel) 7 (2017) 536.
- [69] Y.B. Jeong, T. Wada, S.-H. Joo, J.-M. Park, J. Moon, H.S. Kim, I.V. Okulov, S. H. Park, J.H. Lee, K.B. Kim, H. Kato, Compos. B Eng. 225 (2021), 109266.
- [70] I. McCue, J. Stuckner, M. Murayama, M.J. Demkowicz, Sci. Rep. 8 (2018) 6761.
- [71] N. Wang, Y. Pan, S. Wu, E. Zhang, W. Dai, RSC Adv. 7 (2017) 43255.
- [72] Y.X. Gan, C. Chen, Y.P. Shen, Int. J. Solids Struct. 42 (2005) 6628.
- [73] C. Manière, E. Nigito, L. Durand, A. Weibel, Y. Beynet, C. Estournès, Powder Technol. 320 (2017) 340.
- [74] J. Fu, S.S. Welborn, E. Detsi, ACS Appl. Energy Mater. 5 (2022) 6516.